Constrained Optimization for Safe and Visibility-Aware Shared Control of Magnetically Actuated Microrobots

Leon Raphalen, Marco Ferro, Nicholas R. Posselli, Paolo Robuffo Giordano, *Senior Member, IEEE*, Sarthak Misra, *Senior Member, IEEE*, and Claudio Pacchierotti, *Senior Member, IEEE*

***Abstract*—Safe and intuitive telemanipulation of multiple microrobots is limited by visual occlusions that compromise control and task success. This paper introduces a shared control framework that guarantees safety and visibility by formulating the control problem as a constrained optimization problem. Our framework combines Control Lyapunov Functions (CLFs) for operator-driven stability with High-Order Control Barrier Functions (HOCBFs) to enforce collision and occlusion avoidance, all resolved within a real-time Quadratic Program (QP). A key innovation is a rendering technique based on the QP's Lagrange multipliers, which are used to decompose the optimal control solution. This method isolates the effects of individual constraints to provide the human operator with distinct, interpretable visuo-haptic cues for navigation and avoidance. The architecture also includes a viewpoint optimization system with a virtual autonomous camera to maximize task visibility. The framework is validated via two user studies in simulation and a demonstration on a real-world electromagnetic microrobotics actuation system. Results confirm that our visuo-haptic shared control strategies significantly improve user performance and task completion rates, while the control design provably prevents the microrobots from colliding or entering occluded regions.**

***Note to Practitioners*—Remote manipulation of magnetic microrobots presents significant challenges. Operators frequently struggle with collisions or losing track of the robot within the camera field of view, compromising safety. To counter this, we propose a shared-control architecture that functions as an intelligent assistant. Our algorithm automatically restricts robot motion to prevent collisions and maintain visibility. Moreover, we couple this autonomy with haptic feedback. When the system intervenes to stop an unsafe move, the operator feels a resistive force on the control interface. This feedback provides immediate awareness of system constraints, maintaining operator agency while ensuring safety. Experimental validation demonstrates that this approach reduces task completion time and error rates compared to manual control. We validated the system in a laboratory setting with two microrobots. While not yet deployed in clinical scenarios, this framework lays the groundwork for, e.g., controlling medical tools via ultrasound imaging. Furthermore, these feedback principles extend beyond the micro-scale, offering safety solutions for industrial manipulators in cluttered environments.**

***Index Terms*—Shared control, microrobotics, haptics and haptic interfaces, constrained optimization.**

I. INTRODUCTION

ROBOTIC systems operating at the microscale are becoming increasingly important in domains such as targeted drug delivery, minimally invasive medical procedures, and microassembly [1], [2]. Within this context, micromanipulation, defined as the precise control of interactions with tiny objects in confined environments, stands out as a particularly demanding task for biomedical and manufacturing applications, requiring exceptional dexterity, accuracy, and responsiveness.

Whether addressed through single-robot or multi-robot approaches, with the latter enabling more complex and collaborative interactions [3], micromanipulation strongly relies on *visual monitoring* as a key enabling capability, with vision-based feedback often being the only practical means to track untethered microrobots and evaluate task execution. However, the presence of cluttered environments, manipulated objects, and the robots themselves frequently leads to occlusions that can compromise visibility [4]. Such limitations not only hinder precise control but may also jeopardize the safety and success of the overall task, making occlusion avoidance a central challenge for effective telemanipulation at the microscale.

Traditional solutions mitigate these issues through predictive filtering [5], sensor fusion [6], or expanded visual coverage [7]. However, these approaches can increase operator cognitive load and introduce new challenges in viewpoint selection and scene interpretation. These may be tackled from the observer's side, where viewpoint optimization or immersive virtual reality (VR) setups can stand as viable solutions to improve visibility and situational awareness through virtual environments [8].

Alternatively, these challenges may also be addressed at the control level, ensuring that robots proactively avoid entering occluded regions. In this respect, shared control reveals a practical paradigm to address such limitations by combining

---

Received 1 September 2025; revised 19 December 2025; accepted 14 February 2026. Date of publication 30 March 2026; date of current version 7 April 2026. This article was recommended for publication by Associate Editor H. Wang and Editor L. Zhang upon evaluation of the reviewers' comments. This work was supported in part by EU Horizon Europe R&I Program under Grant 101070066 (project REGO) and in part by French ANR under Grant ANR-20-CHIA-0017 (project MULTISHARED). *(Corresponding author: Leon Raphalen.)*

This work involved human subjects or animals in its research. Approval of all ethical and experimental procedures and protocols was granted by the Inria Ethics Committee under Application No. COERLE n. 344.

Leon Raphalen, Marco Ferro, Paolo Robuffo Giordano, and Claudio Pacchierotti are with CNRS, Inria, IRISA, Université de Rennes, 35000 Rennes, France (e-mail: leon.raphalen@irisa.fr).

Nicholas R. Posselli is with the Surgical Robotics Laboratory, Department of Biomechanical Engineering, University of Twente, 7522 NB Enschede, The Netherlands.

Sarthak Misra is with the Surgical Robotics Laboratory, Department of Biomechanical Engineering, University of 7522 NB Enschede, The Netherlands, and also with the Department of Biomaterials and Biomedical Technology, University Medical Center Groningen, University of Groningen, 9712 CP Groningen, The Netherlands.

This article has supplementary downloadable material available at https://doi.org/10.1109/TASE.2026.3676201, provided by the authors.

Digital Object Identifier 10.1109/TASE.2026.3676201

human intuition with autonomous assistance [9]. This human-in-the-loop approach is especially promising for microscale manipulation, where precise control and intuitive feedback are critical to perform complex tasks in cluttered environments. In this regard, an important aspect lies in the ability to distinguish the different contributions of the shared control action and render them through complementary sensory channels, thereby improving operator awareness of the system behavior [10].

To fully exploit the potential of shared control in microscale telemanipulation, it is essential to rely on control strategies that can rigorously handle safety and performance requirements. Optimization-based control provides a powerful formalism for this purpose, as techniques such as Quadratic Programming (QP) combined with Control Lyapunov Functions (CLFs) and Control Barrier Functions (CBFs) — including high-order variants (HOCBFs) — allow multiple objectives to be pursued simultaneously while guaranteeing *stability*, *safety* and constraint satisfaction [11]. These approaches, well established in macroscale robotics, are now being adapted to the microscale to enable precise telemanipulation in cluttered environments [12], [13], [14]. Yet, to the best of our knowledge, prior constrained optimization–based control methods for microrobotic manipulation have not explicitly addressed also *visibility* challenges, resulting in a lack of unified approaches that simultaneously ensure stability, safety, and occlusion-free operation. Furthermore, in shared-control settings, the additional challenges of separating constraint-wise control contributions and of consistently optimizing user awareness via visuo-haptic feedback remain largely underexplored.

Therefore, in this work, we present a novel visibility-aware, haptic shared-control framework for telemanipulation through multiple untethered electromagnetic microrobots. The operator issues commands via a 6-DoF haptic interface and receives both visual and haptic feedback, enabling safe, precise, and intuitive micromanipulation even in environments populated by obstacles and with complex occlusions. In detail, inspired from [12] and [13], the main contributions of the paper consist in: i) a visibility-aware control formulation, adding a new *visibility* objective within a QP–CLF–CBF framework, to prevent microrobots from entering occluded regions during micromanipulation tasks; ii) a constraint-aware multisensory rendering strategy, where Lagrange multipliers are used to decouple the contributions of individual constraints (e.g., collisions, occlusions) and provide interpretable haptic and visual feedback to the operator; iii) a viewpoint optimization module, that autonomously selects and updates a virtual camera position to maximize scene visibility, complementing the visibility constraints of the controller; and iv) an extended experimental validation, including two user studies comparing multiple rendering modalities (haptic, visual, VR-based) and a hardware demonstration confirming visibility-aware shared control on a real electromagnetic actuation system.

II. Related Work

Early work on human-in-the-loop manipulation of untethered microrobots concentrated on providing the operator with kinesthetic cues while preserving a 1:1 mapping between a desktop haptic device and a single agent. Microscale control is now present in a wide area of applicative fields [1], with representative examples including the haptic control of self-propelled micro-jets [15] and the Hall-effect force–estimation scheme [16]. These works showed the use of real–time force feedback at the microscale, yet the robot motion authority resided entirely with the human and stability issues induced by the large position/force scaling were only partially mitigated. The move toward *shared* haptic control enabled a human operator and an autonomous controller to collaborate in the control of such systems. Examples are the haptic-assisted steering of soft magnetic micro-grippers [17] or the cooperative assembly of magnetic millirobots [18]. Nevertheless, authority arbitration in these systems is usually realised through discrete mode switching (e.g., “free” versus “guided” motion) rather than by a continuous weighting factor. In simulation, Hamdipoor et al. employed forbidden-region virtual fixtures to constrain multiple magnetic nanoparticles inside branched vessels [19], while Zhong et al. demonstrated spatial constraint–based navigation and emergency replanning for magnetic helical microrobots in dynamic environments [20]. A haptic shared control system for *multiple* untethered microrobots was recently presented by Ferro et al. [9]. Their study demonstrated how combining autonomous strategies with haptic guidance can improve navigation performance and user experience, highlighting the importance of transparent authority sharing in cluttered microscale environments. Complementary efforts have explored independent control strategies under global magnetic actuation [21] and data-driven disturbance-rejection control for coordinated motion of closely interacting millirobots [22].

Visibility constraints affecting teleoperated multi-robot systems were already recognised in early work on cooperative camera control [23] and in occlusion-aware path-projection interfaces [24], while recent research has focused on actively eliminating them through shared-control or autonomous view planning. A first line of studies by Rakita et al. introduced real-time optimisation that drives a camera-in-hand robot to positions that maximise task-relevant visibility while respecting kinematic and collision constraints [25]. Controlled user experiments demonstrated significant reductions in completion time and error rates, establishing adaptive viewpoint control as a reliable means of enhancing situational awareness. Building on this, Xiao et al. proposed a viewpoint-optimization framework combining a formal quality metric with risk-aware planning, demonstrated through a tethered “visual assistant” UAV operating in cluttered environments [26]. Subsequent studies showed that optimized external viewpoints can significantly improve expert operator performance [27].

More recently, data-driven approaches have emerged. Jia et al. trained a contrastive neural network on human demonstrations to predict camera poses that preempt occlusions, thereby reducing perceived workload and task time [28]. Chuang et al. extended imitation learning to a bimanual robot equipped with a dedicated vision arm, jointly acquiring manipulation and active-vision policies that keep critical scene elements within view [29]. Parallel efforts focus on operator interfaces that further mitigate occlusion. VR-based teleoperation frameworks with in-hand depth cameras [30] and orbital head-tracked displays [31] give users intuitive, low-

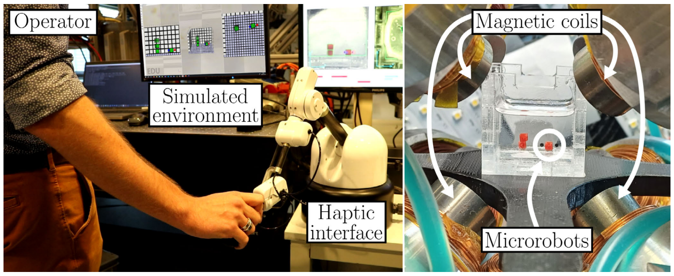

Fig. 1. Integrated shared control system. (Left) An operator uses a 6-DoF haptic interface to teleoperate a pair of microrobots, which are simultaneously rendered in a simulated environment. (Right) A close-up of the real-world BatMag system, showing the electromagnetic coils used to actuate the microrobots within the workspace. Our framework provides the operator with visuo-haptic feedback to guide navigation and ensure safety from collisions and occlusions.

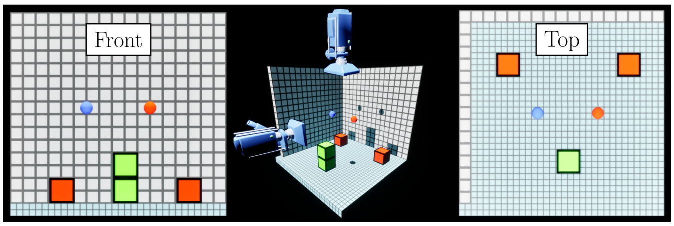

Fig. 2. Simulated micromanipulation environment. The workspace contains two microrobots (blue and red spheres), obstacles (orange cubes), and objects to be manipulated (green cubes). The scene is monitored by two orthogonal cameras providing (left) front and (right) top-down views, which are used for feedback control. (Middle) A three-quarter perspective view is also rendered to enhance the operator's spatial awareness.

latency control of viewpoint selection. Human-factor studies reveal that aligning the control frame with the active view improves efficiency but at the cost of mode-switching overhead [32], while perception-action coupling analyses emphasise the cognitive burden of simultaneous manipulation and camera steering [33].

III. SAFE MULTI-ROBOT CONTROL

A. Problem Formulation

We consider a pair of magnetic, miniaturized spheres (from now on, also referred as "microrobots"), moving within a confined, small-scale workspace under the influence of a controlled magnetic field, and tracked via vision sensors. As a representative platform satisfying these conditions, we consider the BatMag electromagnetic system [34] as a reference for our proposed control approach. This system employs nine electromagnetic coils to generate both magnetic fields and gradients, enabling the independent application of forces at specific points in the workspace to steer the microrobots. The workspace is a cube with side length 22mm, observed by two orthogonally positioned cameras. These cameras triangulate the positions and velocities of the microrobots, provided they remain within the overlapping fields of view.

We aim to enable a human user to teleoperate the pair of microrobots so as to perform a *micromanipulation* task, consisting in grasping and transporting N_O known cube-shaped objects within the workspace to assemble them in a desired way. A virtual rendering of this setup is shown in Fig. 2.

Accomplishing this task under the described conditions is particularly challenging due to the cluttered and constrained nature of the workspace. Indeed, the high density of objects in the confined volume increases the risk of unintended collisions, compromising the integrity of the manipulated items or the microrobots themselves. Additionally, the presence of multiple objects in this space can lead to frequent occlusions, where microrobots can be partially or fully hidden from the cameras. Such visibility losses can undermine the tracking accuracy required for closed-loop control, ultimately degrading system performance or leading to failure in task execution.

Addressing these challenges requires a control strategy that not only drives the microrobots to a desired position with formal guarantees of *stability*, but also ensures *safety* by preventing undesired collisions, and preserves *visibility* by keeping the microrobots continuously within the field of view of the vision sensors. In addition, the strategy should achieve these goals with minimal *control effort*. To this end, we develop an optimization-based control framework based on the QP-CLF-CBF formalism, inspired from [12] and [13] to a solution satisfying the following control objectives:

(O1) *stability*: steer the microrobots to a desired position;
(O2) *safety*: avoid collisions with the environment boundaries, with obstacles, and between microrobots;
(O3) *visibility*: avoid occlusions from obstacles, and between microrobots;
(O4) *control effort*: minimize the applied forces.

In the following analysis, we assume that the microrobots' positions and velocities are available, either from ideal simulated settings or from external visual tracking, as detailed in Sec. VI. The target block to be grasped is explicitly designated to the operator, while all remaining blocks and the partially assembled structure are treated as static obstacles. Visibility is handled using a parallel-projection camera model with two fixed, orthogonally placed cameras.

B. System Modeling and Control Problem Formulation

The magnetic field exerts forces $\boldsymbol{f}_{\mathcal{R},1}, \boldsymbol{f}_{\mathcal{R},2} \in \mathbb{R}^3$ at the microrobots positions $\boldsymbol{p}_1, \boldsymbol{p}_2 \in \mathbb{R}^3$, according to the model:

$$m_i(\ddot{\boldsymbol{p}}_i - \mathbf{g}) + \eta\, \boldsymbol{v}_i = \boldsymbol{f}_{\mathcal{R},i}, \quad i = 1, 2, \tag{1}$$

where m_i is the sphere's mass, $\mathbf{g}$ the gravity vector, η the viscous drag coefficient of the medium, and $\boldsymbol{v}_i = \dot{\boldsymbol{p}}_i$; all states are expressed in the workspace frame $\mathcal{F}_W$. (1) can be written as an affine system $\dot{\boldsymbol{x}} = \boldsymbol{f}(\boldsymbol{x}) + \boldsymbol{h}(\boldsymbol{x})\,\boldsymbol{u}$, with $\boldsymbol{x} = (\boldsymbol{p}_1, \boldsymbol{p}_2, \boldsymbol{v}_1, \boldsymbol{v}_2)^T = (\boldsymbol{p}, \boldsymbol{v})^T \in \mathbb{R}^{12}$ being the state vector, $\boldsymbol{u} = (\boldsymbol{f}_{\mathcal{R},1}, \boldsymbol{f}_{\mathcal{R},2})^T \in \mathbb{R}^6$ the control input; $\boldsymbol{f} : \mathbb{R}^{12} \to \mathbb{R}^{12}$ and $\boldsymbol{h} : \mathbb{R}^{12} \to \mathbb{R}^{12\times 6}$ being locally Lipschitz.

This formulation enables us to cast the objectives (O1–O4) as a QP-CLF-CBF problem [35]. In particular, position-based objectives require a high-order generalization of Control Barrier Functions (HOCBFs) [11], since the force control input must be integrated twice to influence position (i.e., the position has relative degree $\varrho = 2$). Formally, this consists in computing the control inputs for (1) as the solution $\boldsymbol{u}^*$ of an optimization problem that minimizes a quadratic cost function subject to linear inequality constraints in the control input $\boldsymbol{u}$, i.e.,:

$$\boldsymbol{u}^* = \arg\min_{\boldsymbol{u}\in\mathbb{R}^m} \mathcal{C}(\boldsymbol{u}) \quad \text{s.t.} \quad \begin{array}{c} \boldsymbol{A}\boldsymbol{u} \le \boldsymbol{b} \\ \boldsymbol{u}_{lb} \le \boldsymbol{u} \le \boldsymbol{u}_{ub} \end{array}, \tag{2}$$

where $\mathcal{C}(\boldsymbol{u})$ denotes the cost function, $\boldsymbol{A} \in \mathbb{R}^{n\times m}$ and $\boldsymbol{b} \in \mathbb{R}^{n}$ encode n affine inequality constraints, $\boldsymbol{u}_{lb}, \boldsymbol{u}_{ub} \in \mathbb{R}^{m}$ are input lower and upper saturation limits. For our control problem, different constraints will be defined to enforce *stability* (O1) through CLF [36], and *safety* and *visibility* (O2-O3) through HOCBFs [11]. Finally, the cost function $\mathcal{C}(\boldsymbol{u})$ will handle the minimization of the *control effort* (O4).

C. Control Objectives

1) Objective O1 (Stability) - Steering to a Desired Position: Given a pair of reference positions $\boldsymbol{p}_r = (\boldsymbol{p}_{r,1}, \boldsymbol{p}_{r,2})^T$, this objective consists in regulating the system state $\boldsymbol{x}$ to a reference $\boldsymbol{x}_r = \left(\boldsymbol{p}_r, \boldsymbol{v}_r\right)^T$. This is achieved by defining the CLF:

$$V(\boldsymbol{x}) = \frac{1}{2}(\boldsymbol{x}_d - \boldsymbol{x})^T(\boldsymbol{x}_d - \boldsymbol{x}), \tag{3}$$

where $\boldsymbol{x}_d$ is a virtual reference state designed via the *backstepping technique* [37] accounting for the relative degree $\varrho = 2$:

$$\boldsymbol{x}_d = \begin{bmatrix} \boldsymbol{p}_r \\ k_p(\boldsymbol{p}_r - \boldsymbol{p}) + k_v \boldsymbol{v}_r \end{bmatrix}, \; k_p, k_v > 0. \tag{4}$$

2) Objective O2 (Safety) - Avoiding Collisions: This is enforced with respect to the workspace boundaries, obstacles, or other microrobots. Note that since all constraints are position-dependent, they all have relative degree $\varrho = 2$ and, therefore, are addressed using HOCBFs. For each of them, an additional safety margin $\epsilon_\circ$ taking into account potential sensing/actuation errors and loop delays is also included.

Workspace Boundaries: By the geometry of the considered BatMag system [34], the workspace is modeled as a cuboid, with $(\boldsymbol{p}_{\min}, \boldsymbol{p}_{\max})$ denoting its limits; thus, for each microrobot $i = 1, 2$ we require $\boldsymbol{p}_i \in \left[\boldsymbol{p}_{\min}, \boldsymbol{p}_{\max}\right]$. Denoting by $N_{\mathcal{R}} = 2$ the number of microrobots and $N_{dim} = 3$ the space dimensionality, the following set of $2N_{\mathcal{R}}N_{dim} = 12$ barrier candidates, expressed by $\mathcal{W}$, is considered:

$$B_{\mathcal{W},i}(\boldsymbol{x}) = \begin{bmatrix} B_{b^+,i}(\boldsymbol{x}) \\ B_{b^-,i}(\boldsymbol{x}) \end{bmatrix} = \begin{bmatrix} \boldsymbol{p}_i - \boldsymbol{p}_{min} + \epsilon_{\mathcal{W}} \\ \boldsymbol{p}_{max} - \epsilon_{\mathcal{W}} - \boldsymbol{p}_i \end{bmatrix} \in \mathbb{R}^6 \tag{5}$$

Obstacles: For each microrobot i with radius r_i, we define the set $\mathcal{O}$ of the following barrier candidates, targeting obstacle o_j, with $j = 1, \ldots, N_{\mathcal{O}}$ and a collision sphere of radius r_j:

$$B_{\mathcal{O}_{i,j}} = \|\boldsymbol{p}_i - \boldsymbol{p}_{o_j}\| - (r_i + r_{o_j} + \epsilon_{\mathcal{O}}). \tag{6}$$

Mutual Due to dipole-dipole magnetic interactions, microrobots could attract each other and unintendedly collide when their relative distance falls below a critical threshold r_{crit} [9]. To avoid this, we define the barrier candidate:

$$B_{\mathcal{M}}(\boldsymbol{x}) = \|\boldsymbol{p}_1 - \boldsymbol{p}_2\| - d_m, \quad d_m \geq r_{crit} + \epsilon_{\mathcal{M}}. \tag{7}$$

3) Objective O3 (Visibility) - Avoiding Occlusions: Building on the characteristics of the considered setup, we also impose that the microrobots remain free from occlusions in the views of the two orthogonally placed cameras of the BatMag system. For each camera, occlusions are considered both with respect to static workspace objects and to other microrobots. In analogy with the strategy proposed for Objective O2, this requirement is enforced by ensuring that the projection of each microrobot onto a camera's image plane never overlaps with the projection of any potential occluding object, ultimately defining a further set of *visibility* constraints via position-based HOCBFs. Since the camera-to-robot distance is much larger than the microrobots' motion scale, we adopt a parallel projection model: for each microrobot (i) - visual occluder (V_j) - camera (k) combination, the projected mirorobot-occluder distance is computed as $d_{i,j,k}(\boldsymbol{x}) = \|(\boldsymbol{I} - \hat{\boldsymbol{c}}_k\hat{\boldsymbol{c}}_k^T)(\boldsymbol{p}_i - \boldsymbol{p}_{V_j})\|$, where $\boldsymbol{p}_{V_j}$ denotes the position of the occluder and $\hat{\boldsymbol{c}}_k$ is the camera's principal axis. We then denote by $\mathcal{V}$ the set of following barrier candidates associated with each constructed tuple (i, j, k) and defined as

$$B_{\mathcal{V}_{i,j,k}}(\boldsymbol{x}) = \|d_{i,j,k}(\boldsymbol{x})\|^2 - \left(r_i + r_{V_j} + \epsilon_{\mathcal{V}}\right)^2, \tag{8}$$

where r_{V_j} is the radius of the visual occluder bounding circle in the camera image.

4) Objective O4 (Control Effort) - Minimizing the Applied Forces: Provided that the Objectives above are enforced through the inequality constraints, we require the system to minimize the overall *control effort* by introducing the norm of the microrobots' acceleration in the cost function $\mathcal{C}(\boldsymbol{u})$, defined up to a constant κ (irrelevant to the optimization problem):

$$\begin{aligned} \mathcal{C}(\boldsymbol{u}) &:= \sum_{i=1}^{2} \ddot{\boldsymbol{p}}_i^T \ddot{\boldsymbol{p}}_i \\ &= \sum_{i=1}^{2} \frac{1}{m_i^2}\boldsymbol{u}_i^T\boldsymbol{u}_i + \frac{2}{m_i}\left(\mathbf{g} - \frac{\eta}{m_i}\boldsymbol{v}_i\right)^T \boldsymbol{u}_i + \|\mathbf{g} - \frac{\eta}{m_i}\boldsymbol{v}_i\|^2 \\ &= \frac{1}{2}\boldsymbol{u}^T\boldsymbol{H}\boldsymbol{u} + \boldsymbol{c}^T\boldsymbol{u} + \kappa. \end{aligned} \tag{9}$$

D. Optimal Control Formulation

The control Objectives formulated above are finally collected to build the QP-based optimal control problem (2), following the standard formalism layed in seminal [38] and [39]. Possible feasibility issues that could arise between the *stability*, *safety* and *visibility* constraints are handled through the introduction of a *slack* variable δ as auxiliary optimization variable, to relax the *stability* Objective O1 in the CLF formulation with respect to the *safety* and *visibility* Objective O2-O3:

$$\begin{aligned} \boldsymbol{u}^*,\, \delta^* =\; & \arg\min \mathcal{C}(\boldsymbol{u}) + \mu\delta^2 && \text{(O4)} \\ \text{s.t.}\quad & L_f V(\boldsymbol{x}) + L_h V(\boldsymbol{x})\,\boldsymbol{u} + \gamma(V(\boldsymbol{x})) \leq \delta && \text{(O1)} \\ & L_f^2 B_\circ(\boldsymbol{x}) + L_h L_f B_\circ(\boldsymbol{x})\,\boldsymbol{u} \\ & \quad + L_f\alpha_{\circ,1}(B_\circ(\boldsymbol{x})) + \alpha_{\circ,2}(\psi_\circ(\boldsymbol{x})) \geq 0 && \text{(O2,3)} \\ & \boldsymbol{u}_{lb} \leq \boldsymbol{u} \leq \boldsymbol{u}_{ub}, \delta \geq 0 \\ \circ =\; & \left\{\mathcal{W}_i, \mathcal{O}_{i,j}, \mathcal{M}, \mathcal{V}_{i,l,k}\right\} \\ \{i, j, k, l\} =\; & 1, \ldots, \{N_{\mathcal{R}}, N_{\mathcal{O}}, N_{\mathcal{C}}, N_{\mathcal{V}}\} \end{aligned} \tag{10}$$

where: $\gamma()$ and $\alpha_{\circ,m}()$, for $m = 1, \ldots, \varrho = 2$, are extended class-$\mathcal{K}$ functions; $\psi_\circ(\boldsymbol{x}) = \dot{B}_\circ(\boldsymbol{x}) + \alpha_{\circ,1}(B(\boldsymbol{x}))$; $\mu > 0$ is a penalizing factor. The overall number of constraints handled by the designed problem will then be $n_c = N_{\mathcal{R}}(2N_{dim} + N_{\mathcal{O}} + N_{\mathcal{V}}N_{\mathcal{C}}) + \sum_i^{N_{\mathcal{R}}-1} i$, with $N_{\mathcal{R}} = 2$ for a pair of agents, $N_{dim} = 3$ for tridimensional space, and $N_{\mathcal{O}}, N_{\mathcal{V}}, N_{\mathcal{C}}$ the amount of obstacles, visual occluders and cameras, respectively. From here, it is easy to observe that they retain the affine expression from (2) w.r.t. the optimization variables $(\boldsymbol{u}, \delta)^T$. The optimal problem solution $\boldsymbol{u}^*$ can finally be obtained using any standard

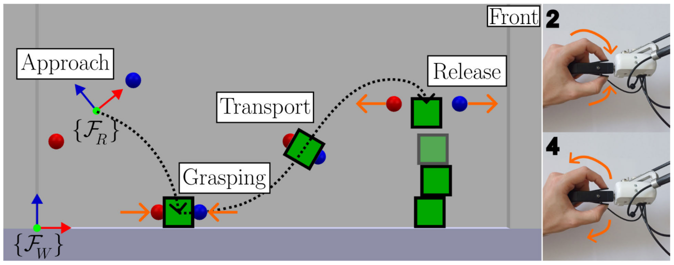

Fig. 3. Four-step collaborative micromanipulation task (*cf. support video at 00:26*). The operator guides the microrobot pair (spheres) to: (1) Approach a target object (green cube). (2) Perform a grasping maneuver, entering the object's indentations. (3) Transport the object to a target location. (4) Release the object to assemble a structure. The user controls the formation frame $\{\mathcal{F}_R\}$via the haptic device to execute these steps.

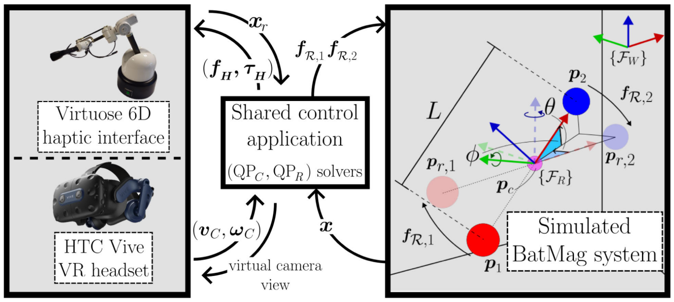

Fig. 4. System workflow. The user provides the reference state $\boldsymbol{x}_r$ through the haptic interface, corresponding to a reference microrobots formation $F_d = \langle \boldsymbol{p}_c, \phi, \theta, L \rangle$, and the simulated environment returns the current state $\boldsymbol{x}$. Our control framework computes, through QP_C and QP_R: i) the optimal forces $\boldsymbol{f}_{\mathcal{R},1-\mathcal{R},2}$ actuating the microrobots from positions $\boldsymbol{p}_{1-2}$; ii) the visuo-haptic sensory feedback provided to the user.

QP solver, with time complexity $O(n_s^3 + n_s^2 n_c + n_s n_c^2)$, where n_s is the amount of states in the control input.

It is worth to note that, when solving a constrained optimization problem as (10), either analytically or via a numerical QP solver, one obtains not only the optimal control input $\boldsymbol{u}^*$ but also the set of optimal *Lagrange multipliers* $\boldsymbol{\lambda}^* \in \mathbb{R}^n_{\geq 0}$, quantifying the influence of each of the n constraints on $\boldsymbol{u}^*$ [40]. In the next Section, we show how this information can be leveraged in a shared-control context for decoupling the contributions of individual constraints in a multisensory rendering strategies, thereby allowing the user benefiting from differentiated feedback about specific corrective actions.

IV. QP-BASED SHARED CONTROL WITH VISUO-HAPTIC FEEDBACK

We extend the proposed control methodology to a shared-control framework for micromanipulation tasks, enabling the autonomous controller and human operator to cooperate in guiding the microrobots. In our target scenario, the microrobots are coordinated to collaboratively grasp, transport, manipulate, and assemble small-scale components, as illustrated in Fig. 3. To support this, we first present the overall shared-control architecture and its teleoperation loop for micromanipulation. We then describe how the intrinsic structure of the QP and its Lagrange multipliers can be exploited to isolate the contributions of individual constraints to the optimal control input, and how this information is conveyed to the operator through integrated visuo-haptic feedback. Finally, we introduce a VR-ready simulation of the reconstructed microscale workspace, supporting both immersive viewpoint control by the user and automated viewpoint optimization, driven by the QP formulation, to maximize microrobot visibility.

A. Shared Control Architecture

With reference to Fig. 4, the proposed shared control setup consists of the following components:

1) Microscale Environment: The system operates within an electromagnetic setup analogous to the BatMag platform, where desired forces are mapped to coil currents to produce the intended actuation of the microrobots. As an alternative, a detailed simulation of this system has been developed using CoppeliaSim and Unreal Engine. In this virtual environment, the built-in physics engines model the microrobots as rigid bodies subjected to bounded forces, abstracting the underlying electromagnetic actuation and current-to-force mapping. This simulation offers flexible scene configuration and seamless integration with external software for control and data streaming.

2) VR Headset: Unreal's native VR rendering is paired with an HTC Vive headset to immerse the operator in the simulated workspace and enhance situational awareness during the micromanipulation task. The headset interfaces with the Unreal Engine environment and uses its internal motion-tracking sensors to capture the translational and rotational velocities of the user's head, $(\boldsymbol{v}_C, \boldsymbol{\omega}_C)$. These measurements are mapped to the motion of an external virtual camera observing the scene, enabling an intuitive first-person experience in which the user can naturally adapt their viewpoint to improve visibility and tailor the observation angle to the task-specific needs.

3) Haptic Interface: A Virtuose 6D (Haption, France) is used to measure the position and orientation of a handheld end-effector in real time, with the handle featuring a pinchable claw at the fingertip for interaction. The device offers full 6D force and torque feedback, allowing the implementation of diverse haptic rendering strategies. These capabilities enable the operator to physically perceive task-relevant information—such as constraint enforcement, thus enriching sensory feedback and improving overall situational awareness during the micromanipulation task.

B. Control Arbitration

To adapt the QP-based control framework (10) to a shared-control setting, we design it so that the combination between the operator's input and the autonomous controller arises from two complementary mechanisms: i) *intrinsically*, by coupling the CLF stability objective to the human teleoperation command; and ii) *configurably*, by assigning specific responsibilities to either the human or the autonomous controller.

Regarding point (i), the intrinsic component of shared control arises from the fact that the human operator continuously provides the reference state $\boldsymbol{x}_r = (\boldsymbol{p}_r, \boldsymbol{v}_r)^T$ in (4) (*cf. support video at 00:51*). To achieve this, the interface's state is mapped to a reference *formation* $F_d = \langle \boldsymbol{p}_c, \phi, \theta, L \rangle$ of the microrobots that identifies the moving reference frame $\mathcal{F}_R$, where $\boldsymbol{p}_c = \frac{1}{2}(\boldsymbol{p}_1 + \boldsymbol{p}_2)$ is the centroid between the microrobots, θ and ϕ are the polar and azimuthal angles of the segment $(\boldsymbol{p}_2 - \boldsymbol{p}_1)$, and $L = \|\boldsymbol{p}_2 - \boldsymbol{p}_1\|$ is their distance (see right inset picture of Fig. 4). Inspired from [41], only one rotation at a time is enabled to reduce cognitive workload in 3D maneuvering, with the switching between the two rotations done through a button on the end-effector of the haptic device. The microrobots' reference position easily follows as $\boldsymbol{p}_{r,i} = \boldsymbol{p}_c \pm \frac{L}{2}(\cos\phi\cos\theta, \cos\phi\sin\theta, \sin\phi)^T$, with the reference velocity $\boldsymbol{v}_{r,i}$ flawlessly obtained by differentiation. Finally, the grasping manoeuvre is then initiated by gradually closing the pinchable claw of the haptic device, mapped to L in the reference formation F_d: as the operator reduces L, the two microrobots approach each other until they establish contact with the block surfaces. This operator-defined reference directly enters the CLF constraint (3), and the autonomous controller regulates the system toward it through the QP solution to enforce *stability*, defining the nominal behavior in the absence of additional active constraints.

Regarding point (ii), the configurable component of shared control arises from the flexible assignment of the HOCBF *safety* and *visibility* constraints (5)–(6), which ultimately determines the arbitration between the human intent and the autonomous intervention. Inspired by [12], this is achieved by defining a *dual* QP formulation, which leverages two separate instances of the QP problem (10): QP_C, defined on the *current* microrobot state, and QP_R, defined on the operator-specified *reference* state. Constraints assigned to QP_C are autonomously enforced and directly shape the optimal control input $\boldsymbol{u}^*$, thus determining the autonomous corrective action. In contrast, constraints assigned to QP_R, generate contributions that are coherent with the operator's intended motion and are therefore suitable for visuo-haptic rendering. Allocating each constraint to a specific QP instance allows then the system designer to choose which constraints are handled autonomously and which are conveyed to the operator as guidance cues. This mechanism relies on the ability to isolate constraint contributions, detailed in Sec. IV-C, and determines the corresponding feedback modalities, further discussed in Sec. IV-D.

C. Constraint-Wise Optimal Input Decoupling

1) Closed-Form Expression of the QP Solution: For the generic optimization problem in (2) with cost (9), the optimal input $\boldsymbol{u}^*$ can be obtained in from the Karush–Kuhn–Tucker (KKT) conditions of the associated Lagrangian $\mathcal{L}(\boldsymbol{u}, \boldsymbol{\lambda})$, where $\boldsymbol{\lambda} \in \mathbb{R}^n_{>0}$ is the vector of Lagrange multipliers for the n inequality constraints [40]. This yields the closed form expression of the optimal solution as

$$\boldsymbol{u}^* = -\boldsymbol{H}^{-1}\left(\boldsymbol{c} + \sum_{i=1}^{n} \lambda_i^* \boldsymbol{A}_i^T\right), \tag{11}$$

where $\boldsymbol{A}_i$ denotes the i-th row of $\boldsymbol{A}$ in (2), and λ_i^* is the optimal Lagrange multiplier associated with constraint i.

2) Constraint-Wise Decomposition of Control Inputs: This closed-form expression naturally separates the optimal solution into individual constraint contributions. Each term $\lambda_i^* \boldsymbol{A}_i^T$ points in the direction in which constraint i influences $\boldsymbol{u}^*$, and its magnitude encodes its relative strength. We therefore define the input contribution of constraint i and the combined contribution of any set of constraints $\mathcal{S}$ as

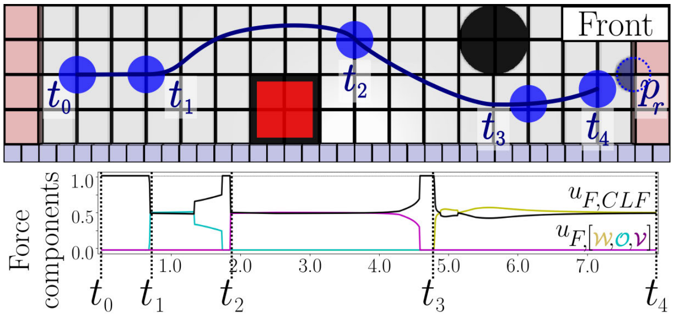

Fig. 5. Constraint isolation (*cf. support video at 01:16*). Top: a single microrobot (solid blue circle) is given a reference state at a position p_r (transparent), requiring to traverse an obstacle (red square), an occlusion spot (black circle) and to approach a workspace boundary (pink). Bottom: normalized contributions (summing up to 1.0) resulting from the CLF constraint (3) (black, *CLF*) and from the HOCBF constraints for workspace boundary ($\mathcal{W}$), obstacle ($\mathcal{O}$) and visual occlusion ($\mathcal{V}$) avoidance (in yellow, cyan and magenta, respectively), over the path towards the reference. The highlighted time instants indicate the trigger moments at which the different contributions become active: at t_0, the microrobot is in a safe region and subject only to the CLF contribution by $\boldsymbol{u}_{F,CLF}$; at t_1, the microrobot approaches an obstacle and the corresponding avoidance constraint activates, yielding a non-zero $\boldsymbol{u}_{F,\mathcal{O}}$; at t_2, the microrobot approaches an occluded area, enabling the visibility constraint and causing a non-zero $\boldsymbol{u}_{F,\mathcal{V}}$; at t_3, the microrobot approaches the boundary of the workspace, triggering a non-zero $\boldsymbol{u}_{F,\mathcal{W}}$; finally at t_4, the microrobot has reached a force equilibrium between the CLF attracting it towards its target state and the HOCBF repulsing it from the wall, effectively remaining safely stationary as close as possible.

$$\boldsymbol{u}_i = -\boldsymbol{H}^{-1}\lambda_i^* \boldsymbol{A}_i^T, \boldsymbol{u}_\mathcal{S} = \sum_{i \in \mathcal{S}} \boldsymbol{u}_i \tag{12}$$

where $\boldsymbol{u}_i$ represents the portion of the control action induced by constraint i, while $\boldsymbol{u}_\mathcal{S}$ aggregates the contributions of all constraints in $\mathcal{S}$. From the QP problem in (10), this decomposition yields $\boldsymbol{u}_1 = (\boldsymbol{f}_{CLF,1}, \boldsymbol{f}_{CLF,2})$, corresponding to the CLF constraint (3) achieving objective O1; similarly, groupings can be defined for any constraint set $\mathcal{S} \in \{\mathcal{W}, \mathcal{O}, \mathcal{V}\}$ related to objectives O2–O3 (see Fig. 5). Note that, since the λ_i scale with their associated constraints, we interpret them only through the resulting constraint-wise control input contributions, rather than as standalone quantities, underlining which constraint contributes most to the full optimal solution.

3) Normalization for Feedback Rendering: Because the extracted contributions are later conveyed to the operator through different feedback modalities, it is useful to normalize them into a consistent scale. For any contribution $\boldsymbol{u}_\diamond$ defined as in (12), we define the rendered feedback term $\boldsymbol{u}_{F,\diamond} = \frac{\boldsymbol{u}_\diamond}{\sum_{i \in \mathcal{S}} \|\boldsymbol{u}_i\|}$, which expresses $\boldsymbol{u}_\diamond$ as its relative share among all active constraints in $\mathcal{S}$. Fig. 5 illustrates a typical scenario in which different constraints become active along the robot's trajectory, and their normalized contributions are isolated through this decoupling approach.

D. Visuo-Haptic Sensory Feedback

The constraint isolation mechanism introduced in the previous Section enables the decomposition of the optimal input into contributions associated with individual objectives. This property is central for shared-control micromanipulation tasks, as it provides a solid basis to generate separate multisensory feedback that enhances the operator's sensing capabilities and situational awareness.

In our framework, we pursue two distinct feedback objectives: i) *current-state feedback*, to improve the operator's understanding of the present condition of the controlled system, as well as of the relative influence of the active objectives; ii) *planning-oriented feedback*, to improve the operator's ability to anticipate or react to critical, potentially unsafe states. To rigorously enforce both feedback objectives, we leverage the *dual* QP formulation detailed in Sec. IV-B. Indeed, by applying the constraint isolation mechanism to either $\mathrm{QP_C}$ or $\mathrm{QP_R}$, we can selectively generate feedback aimed at improving either situational awareness (current-state feedback) or anticipatory decision-making (planning-oriented feedback), through visual or haptic feedback provided to the user (*cf. support video at 01:40*). The feedback generation process is identical for either QP instance, as described next.

1) Haptic Feedback: Any pair of Cartesian input contributions $(\boldsymbol{f}_{u,1}, \boldsymbol{f}_{u,2})$, whether obtained directly from the optimal solution of (10) or via the constraint-isolation decomposition in (12), can be combined to generate a 6D wrench $(\boldsymbol{f}_H, \boldsymbol{\tau}_H)$ rendered to the operator through the Virtuose 6D interface:

$$\boldsymbol{f}_H = s_f \sum_{i=1}^{2} \boldsymbol{f}_{u,i}, \quad \boldsymbol{\tau}_H = s_\tau \sum_{i=1}^{2} (\boldsymbol{p}_i - \boldsymbol{p}_c) \times \boldsymbol{f}_{u,i} \tag{13}$$

where $s_f, s_\tau \geq 0$ are appropriate scaling factors.

2) Visual Feedback: As a complementary modality, we render input contributions as oriented, length-varying arrows in the virtual environment, anchored at either the current positions $(\boldsymbol{p}_1, \boldsymbol{p}_2)$ or the reference positions $(\boldsymbol{p}_{r,1}, \boldsymbol{p}_{r,2})$ depending on the chosen feedback objective (current-state vs. planning-oriented). For the microrobot i, denoting with u_{ub} the upper bound on the control-input magnitude, the arrow direction is aligned to the direction of $\boldsymbol{f}_{u,i}$, while its length is updated as $\ell_i = \min\left\{ \frac{l_{\max}}{u_{ub}} \|\boldsymbol{f}_{u,i}\|, l_{\max} \right\}$, where $l_{\max}$ is the maximum arrow length. Recalling Eq. (12), this scheme applies uniformly to both per-constraint and aggregated objective-level visualizations, under the same normalization principle.

V. VIRTUAL CAMERA VIEWPOINT OPTIMIZATION

To further enhance the operator's understanding of the remote microscale scene during micromanipulation tasks, we introduce a viewpoint optimization strategy for the virtual camera in the simulation environment. While visual perception has thus far been improved, as shown in Sec. IV, through the rendering of input-contribution cues and by employing a VR-ready setup for immersive exploration, we now provide also a complementary approach, where the responsibility of avoiding occlusion scenarios is assigned to the observing virtual camera. For this purpose, we formulate the problem within the same optimization-based framework, that adjusts the camera viewpoint autonomously to maximize the visibility of the microrobots and ensure they remain observable in the image plane throughout task execution.

A. Problem Formulation

We consider a virtual camera observing the scene in the simulation environment from an external perspective and oriented toward the center of the cuboid workspace. The objective is to control the camera pose (position and orientation) by computing suitable velocity inputs that drive it to the *optimal viewpoint* configuration, i.e., where the camera view maximizes the visibility of the microrobots in the image plane. At each time step k, given the state of the environment (i.e., microrobot positions and object poses), the viewpoint optimization procedure consists of two stages: i) identify the camera pose of the optimal viewpoint, as the configuration that minimizes the cumulative occlusion distance between each microrobot and all potential occluders, and ii) generate velocity-based control inputs to smoothly drive the camera from its current pose toward the identified one, while maintaining a safe visibility distance from the center of the scene.

B. Identification of the Camera Pose

To determine the camera pose with the *optimal viewpoint* that maximizes microrobot visibility, we adopt a sampling-based view search approach. This strategy evaluates a discrete set of candidate viewpoints around the workspace and selects the one that best preserves visibility while favoring smooth camera transitions. The procedure unfolds as follows:

1) A set of candidate camera positions is sampled around the workspace;
2) For each candidate, the projected distances between each microrobot and all occluding objects are computed;
3) For each candidate, the smallest projected distance is retained, weighted by the distance from the current camera pose to promote smooth transitions, and the candidate with the highest score is selected as the optimal viewpoint.

1) Sample Position Generation: To ensure a homogeneous distribution of viewpoints over the sphere encompassing the workspace, candidate camera positions are generated using a spiraling Young–Fibonacci lattice [42]. This method exploits the quasi-uniform spacing properties of the golden ratio to avoid clustering. In detail, for an odd number of samples $P = 2N + 1$, the spherical coordinates $\boldsymbol{s}_k$ of the k-th sample are defined as

$$\boldsymbol{s}_k = \begin{pmatrix} \mathrm{lat}_k \\ \mathrm{lon}_k \end{pmatrix} = \begin{pmatrix} \arcsin\left(\frac{2k}{2N+1}\right) \\ \frac{2\pi}{\Phi} k \end{pmatrix} \qquad k = -N, \ldots, N. \tag{14}$$

Each pair (lat_i, lon_i), together with a scaling radius r_{vc} defining the distance from the workspace center, uniquely specifies a candidate camera position $\boldsymbol{p}_{\mathrm{vc},k} = \boldsymbol{p}_{\mathrm{vc},k}(\boldsymbol{s}_k, r_{\mathrm{vc}})$, which will be evaluated in the following step.

2) Occlusion Distance Evaluation: Analogously to Sec. III-C, we define a projected distance $d_{i,j,k}$ between a microrobot i and a potential occluding object j from the viewpoint of a sampling position $\boldsymbol{p}_{\mathrm{vc},k}$. The projection is taken along the principal axis $\hat{\boldsymbol{c}}_k = \boldsymbol{c}_k / \|\boldsymbol{c}_k\|$, $\boldsymbol{c}_k = 0.5(\boldsymbol{p}_{\min} + \boldsymbol{p}_{\max}) - \boldsymbol{p}_{\mathrm{vc},k}$, which corresponds to the normalized direction from the sampling point $\boldsymbol{p}_{\mathrm{vc},k}$ to the center of the workspace. The projected distance is then

$$d_{i,j,k}(\boldsymbol{x}) = \left\| (\boldsymbol{I} - \hat{\boldsymbol{c}}_k \hat{\boldsymbol{c}}_k^T)(\boldsymbol{p}_i - \boldsymbol{p}_j) \right\| . \tag{15}$$

To focus exclusively on microrobot visibility, only triplets (i, j, k) where the microrobot i lies farther than the object j along the viewing direction $\hat{\boldsymbol{c}}_k$ are considered, as these correspond to potential occlusion cases.

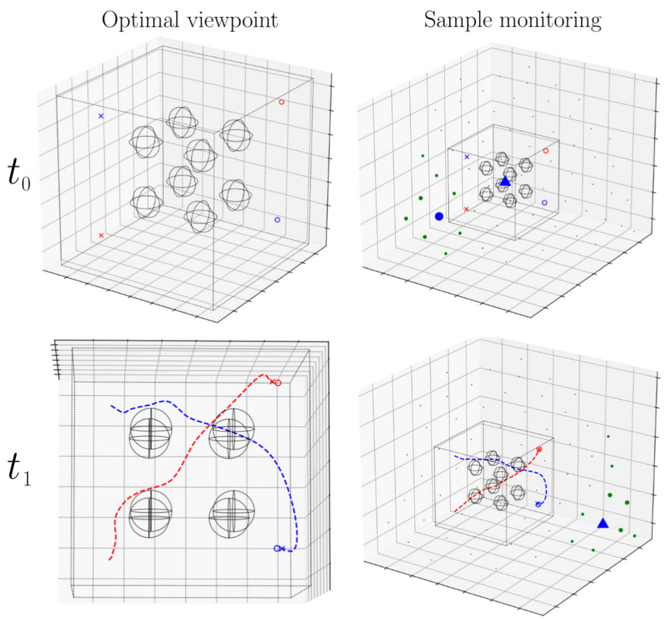

Fig. 6. Viewpoint optimization (*cf. support video at 01:56*). The left images display the scene for the current position of the virtual camera; the right images, the viewpoint samples around the scene. The size of the dots indicate the relative score of the samples; invalid ones are colored red, while the optimal one is blue. The current position of the virtual camera is marked by a blue triangle. The workspace is a $15 \times 15 \times 15$mm cuboid; two microrobots (blue, red crosses) are given a reference state (blue, red circles) on the other side of a workspace containing visual occluders (black wired spheres). Samples are only evaluated in a one-eighth spherical cap surrounding the scene to constraint the camera positions. At t_0, the camera is initialized from a three-quarter viewpoint, with the initial optimal viewpoint being on the same side of the agents. As they cross the scene, they pass through partially-occluded areas, with the virtual camera following them while maximizing their visibility until they have fully traversed the workspace at t_1.

3) Sample Score Computation: For each camera sample k, a visibility score S_k is computed to quantify the robustness of the viewpoint against potential occlusions.

First, among all microrobot–occluder pairs (i, j) observed from sample k, we compute the projected distances $d_{i,j,k}$. The smallest of these distances, $d_{\min,k} = \min_{i,j} d_{i,j,k}$, represents the critical visibility margin for sample k, i.e., how close the formation is to being occluded.

Second, this margin is combined with a weighting term that accounts for the spatial displacement between the current camera position $\boldsymbol{p}_{\text{vc}}(t)$ and the candidate $\boldsymbol{p}_{\text{vc},k}$. Specifically, denoting this displacement as $d_k = \|\boldsymbol{p}_{\text{vc}}(t) - \boldsymbol{p}_{\text{vc},k}\|$, the weight is evaluated through a smooth cosine-based shaping function

$$w(d_k) = \frac{1}{2}\left(1 + \cos\left(\frac{d_k - d_{\min}}{d_{\max} - d_{\min}}\pi\right)\right)(w_{\max} - w_{\min}) + w_{\min}, \quad (16)$$

where $d_{\min}$ and $d_{\max}$ denote the minimum and maximum camera-sample distances across all candidates, and $w_{\min}, w_{\max}$ are tuning parameters. This weighting favors candidate viewpoints that are closer to the current camera position, while still preserving robustness against occlusions.

The visibility score for sample k is finally defined as

$$S_k = d_{\min,k} \cdot w(d_k), \quad (17)$$

thereby balancing robustness against occlusions with smoothness of the viewpoint trajectory. Once the scores have been evaluated for all candidate viewpoints, the optimal camera position is determined as the maximizer of the visibility score

$$\boldsymbol{p}_{\text{vc},*} = \arg\max_k S_k, \quad (18)$$

thus ensuring that the selected viewpoint provides maximal robustness to occlusions while promoting smooth transitions from the current camera pose. Fig. 6 displays a rendering of the sample distribution, their score, and the related viewpoint along a nominal autonomous workspace-crossing scenario.

C. Velocity-Based Camera Control

The camera is modeled as a free-flying, velocity-controlled object. To regulate its motion, we employ an optimization-based QP-CLF-CBF framework analogous to the one shown in Sec. III for the microrobot control during. Specifically, the control problem consists of a CLF that drives the camera toward the selected target position $\boldsymbol{p}_{\text{vc},*}$, complemented by a CBF that constrains its motion to remain outside a sampling sphere of radius r_{cam} centered at the workspace. The formal expressions of these functions can be derived similarly to the ones shown in Sec. III-C. The quadratic cost function is finally chosen as $C(\boldsymbol{v}) = \boldsymbol{v}^T\boldsymbol{v}$, with control bounds $\boldsymbol{v} \in [\boldsymbol{v}_{lb}, \boldsymbol{v}_{ub}]$. Solving the corresponding QP yields the optimal camera velocity input that ensures convergence to the desired viewpoint while maintaining safe positioning.

VI. EXPERIMENTAL EVALUATION

We carried out three experimental validation sessions to evaluate the efficiency of our shared control framework, including the control scheme proposed in Sec. III-A, the feedback strategies presented in Sec. IV-D and the viewpoint optimization described in Sec. V. The sessions comprise two user studies in simulation, presented in Sec. VI-B and Sec. VI-C, and one real-world demonstration using the BatMag system [34], presented in Sec. VI-D.

In the simulated validations, full state information (i.e., microrobots' position and velocity) is assumed to be available. In the real-world demonstration with the BatMag system, instead, the positions of the microrobots and of the manipulable blocks are estimated through a vision-based detection module, processing images acquired from the two cameras. The corresponding three-dimensional coordinates are reconstructed via geometric triangulation, while microrobot velocities are obtained through filtered numerical differentiation.

A. Experimental Set-up

The control problem (10) was solved using the QRQP solver within CasADi, executed on an MSI GP66 Leopard laptop equipped with an Intel i7-10870H CPU. The QP solvers ran at a 7.4 ± 4.3 kHz frequency, while the haptic interface was constrained to 1 kHz and the microscale environments (both in simulation and in the real-world) to 25 Hz, in accordance with the hardware specifications of [34]. These high control rates, along with the conservative safety margins accounted in the HOCBF constraints, mitigate together the discrepancies between the conceived continuous-time control framework and its discrete-time implementation,

TABLE I

EXPERIMENTAL PARAMETERS

Global parameters		$\mathrm{QP_C}$-specific		$\mathrm{QP_R}$-specific	
d_m	5.0×10^{-4} m	γ	1.0	γ	5.0
k_p	1.0	$k_{\alpha_1,\circ}$	1.0	$k_{\alpha_1,\circ}$	1.0
k_v	10^{-1}	$k_{\alpha_{2,b_i}}$	10^8	$k_{\alpha_{2,b_i}}$	10^8
L	5.0×10^{-3} m	$k_{\alpha_{2,o_{i,j}}}$	10^{12}	$k_{\alpha_{2,o_{i,j}}}$	10^6
m	5.0×10^{-3} g	$k_{\alpha_{2,m}}$	10^{12}	$k_{\alpha_{2,m}}$	10^{12}
r_i	5.0×10^{-4} m	$k_{\alpha_{2,v_{i,l,k}}}$	10^{15}	$k_{\alpha_{2,v_{i,l,k}}}$	10^5
r_{O_j}	8.7×10^{-4} m	μ	10.0	μ	10.0
$s_{f,\tau}$	1.0	$u_{ub,lb}$	$\pm 10^{-5} N$	$u_{ub,lb}$	$\pm 5.0 N$

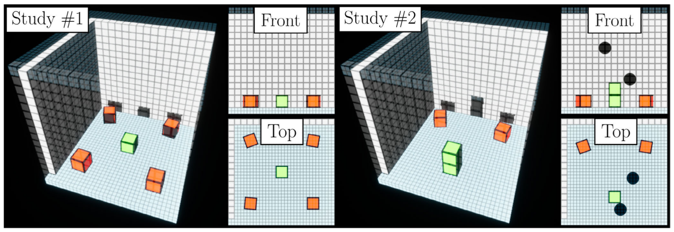

Fig. 7. Study scenes. While only the first user study had combinations featuring the orthogonal viewpoints, both are displayed here to highlight the occlusions phenomena. In particular, Study #1 featured objects occluding each others, and Study #2 introduced dedicated occluded areas in the form of black circles in the camera planes, representing fully occluded zones in the images.

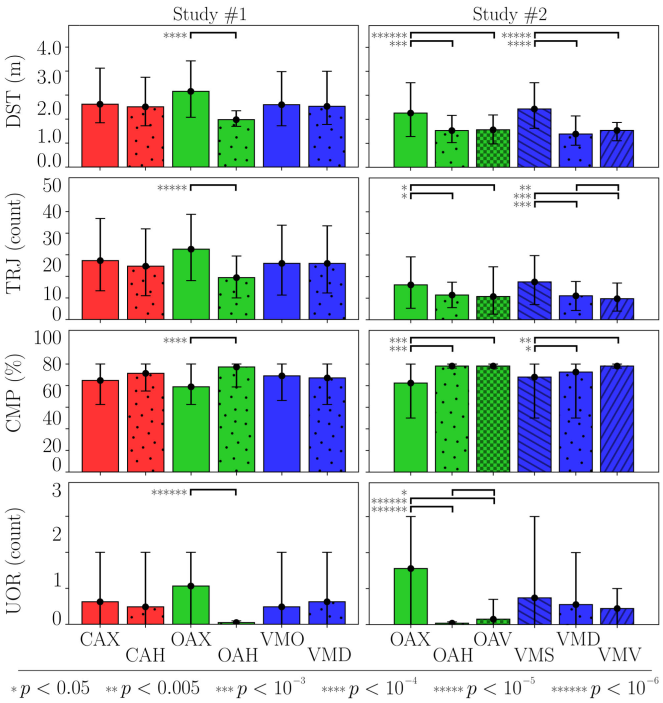

Fig. 8. User study results. Only the metrics common to both experiments are displayed; the study-specific metrics for unintended collision counts and microrobot control focus are detailed in Sec. VI-B and Sec. VI-C, respectively. Only significant p-values (<0.05) are shown.

ultimately allowing to closely approximate the continuous-time guarantees. All HOCBF are shaped with $\alpha_{\circ,1}(B_\circ) = k_{\alpha_1,\circ} \cdot B_\circ$ and $\alpha_{\circ,2}(\psi_\circ) = k_{\alpha_2,\circ} \cdot \psi_\circ^3$, with $k_{\alpha_1,\circ}, k_{\alpha_2,\circ} > 0$. The experiments were conducted with the parameter set available in Tab. I unless specified otherwise. The parameters were initialized based on dimensional considerations and subsequently refined empirically to balance tracking responsiveness with strict enforcement of safety/visibility constraints, with prioritization handled through the slack-variable mechanism. Consistently with seminal works in this area and related applications [35], [43], practical tuning proceeded by first selecting safety margins according to nominal sensing and actuation characteristics, then choosing the CBF gains such that barrier reacts before margin violation under maximum expected velocities, and finally tuning (γ, μ) to achieve a safe yet effective teleoperation behavior while preserving QP feasibility during constraint activation.

The user studies, detailed in Sec. VI-B and Sec. VI-C, were conducted in a simulated workspace, arranged differently according to the study, as shown in Fig. 7. Each simulated scene replicated the cubic workspace of the BatMag system and included a predefined number of cubics blocks placed on its bottom surface. To facilitate stable grasping and prevent undesired slippage during transportation maneuvers, the blocks were fabricated with hemispherical indentations on their lateral faces, allowing the microrobots to be smoothly accommodated and to maintain secure contact throughout manipulation, as can be seen in Fig. 3. Particularly for the second user study, detailed in Sec. VI-C, visibility conditions were made more challenging by including additional artificial, circular occlusion spots, to better emulate constrained visual environments.

In both scenarios, participants performed a microassembly task similar to the one described in [12] and [13], consisting of grasping, transporting, and stacking the blocks to build a tower (see Fig. 3). The task was repeated multiple times under different combinations of autonomous and haptic assistance. Depending on the combination, specific constraints from the control formulation (10) were selectively enabled or disabled in one of the two QP instances ($\mathrm{QP_C}$ and $\mathrm{QP_R}$). To guarantee continuous visibility, the constraints $B_{\mathcal{V}_{i,j,k}}$ (8), which enforce the *visibility* objective O3 in Sec. III-C, were always active in $\mathrm{QP_C}$, ensuring autonomous avoidance of occlusions. Consequently, no complete occlusions of either robot occurred in any of the experiments.

For both studies, performance was assessed using metrics related to operator motion and task execution. For the former, we considered the traveled distance (DST, [m]) and trajectory changes (TRJ, [$\varnothing$]); for the latter, the completion time (CMP, [s]) and unintended object release (UOR, [$\varnothing$]), defined as the accidental drop of a block during transport. Additional study-specific metrics, detailed in Sec. VI-B and Sec. VI-C, were also included in the evaluation. Finally, participants provided subjective feedback on their experience with the system, both between tasks and after completing the entire experiment.

Metrics were analyzed using repeated-measures ANOVA with a significance threshold of $p \leq 0.05$. Sphericity was assumed for variables with only two levels of repeated measures, and a Greenhouse-Geisser correction was applied when the assumption of sphericity was violated. Comprehensive post hoc results with Bonferroni adjustments are reported in Fig. 8.

Notably, the experimental protocol included an extensive tutorial phase (three iterations of six minutes), aimed at letting the users familiarize with the framework with conditions that differed from the actual user study; a latin square randomization of the combinations order was also used to avoid progress bias. This process ensured that the participants were sufficiently used to the system prior to running the studies, effectively clearing a training effect from the results - statistical analysis revealed no significant p-value related to the progress along the experiment for all of the aforementioned metrics.

B. Study #1: Haptic Feedback and Viewpoint Optimization

The virtual environment for the first user study was arranged as shown in the left image of Fig. 7. Five cube-shaped blocks were placed on the floor of the workspace at random positions, which in many cases led to challenging visibility conditions from the two orthogonally placed system cameras, due to mutual occlusions among the blocks. To enhance the user's situational awareness, an additional virtual camera (not part of the original BatMag setup) was introduced to provide a 3D external view of the workspace.

The objective of this study was to evaluate the effectiveness of the shared control and rendering strategies for collision and occlusion avoidance (Sec. IV), as well as to assess the performance of the virtual viewpoint optimization procedure (Sec. V). A total of 16 participants (4 females, 12 males, aged 24–32) took part in the study; more than half reported using haptic or shared control systems less than once per year.

1) Experimental Conditions: We considered the following 6 experimental conditions, resulting in 8 total combinations:

- *Collision avoidance*: i) CAX: no collision avoidance feedback is provided to the user ($B_{\mathcal{W}}, B_{\mathcal{O}}$ are omitted from QP_{R}); ii) CAH: haptic feedback repels the user from collisions ($B_{\mathcal{W}}, B_{\mathcal{O}}$ are included in QP_{R});
- *Occlusion avoidance*: i) OAX: no occlusion avoidance feedback is provided to the user ($B_{\mathcal{V}}$ is omitted from QP_{R}); ii) OAH: haptic feedback repels the user from occlusion spots ($B_{\mathcal{V}}$ is included in QP_{R});
- *Visualization mode*: i) VMO: three separated views, resulting from the two orthogonal views of the system cameras + one static 3D view from the external virtual camera; ii) VMD: one single view from a dynamically moving virtual camera, whose viewpoint is determined by the optimization method in Sec. V.

As a study-specific metric, we also recorded the number of unintended collisions with objects in the workspace.

2) Results Highlights:

- DST, TRJ: with OAH, users followed paths that were $36 \pm 3\%$ shorter ($p < 10^{-4}$) and changed trajectory $41 \pm 9\%$ less frequently ($p < 10^{-5}$);
- CMP: haptic feedback (CAH and OAH) reduced task completion time by $23 \pm 6\%$, with the best performance obtained when both were combined;
- UOR: with OAH, unintended releases were avoided in 95% of the tasks, compared to only 27% without occlusion feedback (OAX);
- CAH eliminated undesired collisions ($p < 10^{-8}$);
- Visualization mode: performance metrics under the optimized single-view VMD condition were not statistically different from those obtained with the three-view VMO setup, indicating that the autonomous camera provided a comparable level of situational awareness while requiring the user to monitor only a single viewpoint ($F(\text{VM}) < 10^{-3} F(\text{CA}, \text{OA})$).

These findings demonstrate that the proposed shared control framework not only guarantees the safety of the microrobotic system but also improves task execution through the integration of haptic feedback. Furthermore, the autonomous viewpoint optimization yielded performance comparable to the combined three-view setup, an important result suggesting that user cognitive load can be reduced by consolidating three views into one without compromising performance.

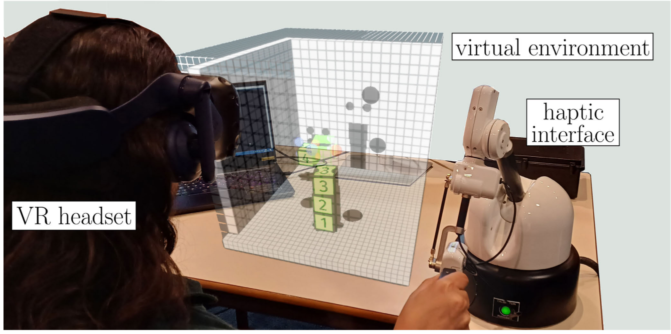

Fig. 9. The considered VR setup. The user performs a micromanipulation task with the haptic interface while wearing a VR headset. The device lets the operator monitor the scene from a first-person perspective, providing them with full control over the viewpoint during the execution of the task.

C. Study #2: Visual Feedback and VR-Based Viewpoint Control

The virtual environment for the second user study was arranged as shown in the right image of Fig. 7. Four cube-shaped blocks were placed on the floor of the workspace at random positions, again resulting in challenging visibility conditions from the two orthogonally placed system cameras due to mutual occlusions among the blocks. To further increase the difficulty, two circular occlusion spots were added to each camera image plane, randomly repositioned in every trial, to emulate a densely populated environment where arbitrary elements could obstruct the camera views. As in the first study, an additional virtual camera was included to provide a 3D external view of the workspace.

The goal of this second study was to compare different rendering modalities for enhancing occlusion avoidance through haptic or visual feedback, and to evaluate the effectiveness of the viewpoint optimization method against an immersive virtual reality (VR) setup, where the user could directly control the viewpoint of the simulated environment.

Fig. 9 shows a participant performing a typical task in VR. A total of 18 participants (3 females, 15 males, age span 23–30) took part in the study. More than half reported using shared control systems less than once per year, and haptic or VR systems less than once per month.

1) Experimental Conditions: We considered 6 experimental factors, resulting in 9 total combinations:

- *Occlusion avoidance*: i) OAX: no occlusion avoidance feedback is provided to the user ($B_{\mathcal{V}}$ is omitted from QP_{R}); ii) OAH: haptic feedback repels the user from occluded areas ($B_{\mathcal{V}}$ is included in QP_{R} and rendered through the haptic interface); iii) OAV: visual feedback hints to the user in which direction to best avoid occluded areas ($B_{\mathcal{V}}$ is included in QP_{R} and rendered visually in the rendered workspace)
- *Visualization mode*: i) VMS: static 3D view from the external virtual camera; ii) VMD: dynamic 3D view

from the external virtual camera, whose viewpoint is optimized as described in Sec. V; iii) VMV: immersive, user-controlled view from the VR headset.

As a study-specific metric, we also recorded distribution of attractive and repulsive components of the microrobot actuation forces, as an indicator of how effectively the operator planned safe trajectories when receiving occlusion avoidance feedback.

2) Results Highlights:

- DST, TRJ: occlusion avoidance feedbacks (OAH and OAV) led to 34 ± 2% shorter paths ($p < 10^{-5}$) and $32 \pm 3\%$ fewer trajectory changes ($p < 0.007$). Non-static visualization modes (VMD, VMV) produced similar improvements, reducing DST by 37 ± 2% ($p < 10^{-5}$) and TRJ by 34 ± 2% ($p < 10^{-3}$);
- CMP: occlusion avoidance feedbacks also accelerated task progress by 23 ± 12% ($p < 0.003$), with 96% of the tasks completed under OA feedback, vs. 63% without;
- UOR: OAH and OAV significantly reduced unintended releases, which occurred in only 7% of tasks when either was active, versus 85% without occlusion avoidance feedback ($p < 10^{-11}$);
- Trajectory safety improvement: OAH outperformed OAV by +5 ± 3% in focusing control effort on teleoperation, reaching up to 72% attractive feedback, whereas in OAX 69±7% of the motion was dedicated to maintaining safety ($p < 10^{-6}$);
- Visualization mode: VMV outperformed VMD in completion time, achieving 56 ± 4% and 20 ± 3% faster execution relative to VMS, respectively ($p < 10^{-9}$);
- Subjective assessment: non-static visualization modes also reduced perceived difficulty ($p < 10^{-8}$) and workload ($p < 10^{-8}$), with participants ranking VMV, VMD, VMS from most to least effective.

Overall, these findings highlight complementary effects of the two types of conditions. Occlusion avoidance feedbacks improved task planning and safety, enabling users to better adapt to workspace constraints, make fewer errors, and complete more tasks successfully. Visualization modes mainly influenced task execution speed and user perception, with enhanced views allowing participants to accomplish the task faster while finding it easier and less demanding.

D. Real-World System Demonstration

As a final validation, we demonstrated our control framework on the physical BatMag system to assess its applicability on real hardware and its robustness to unmodeled dynamics and sensor noise. This experiment served as a proof-of-concept for the controller's real-world viability and robustness to model uncertainties. The following scenarios were chosen to specifically demonstrate the successful hardware implementation of the framework's core safety features, particularly the autonomous and haptic guidance for occlusion avoidance.

The experimental setup extended the one described in Sec. VI-A. The electromagnetic actuation system was interfaced with our shared control framework via a UDP connection, to send the vision-based reconstructed system's state. In turn, the controller computed the array of input forces and sent them back to the system for actuation, enabling microrobot motion. The overall setup is shown in Fig. 1.

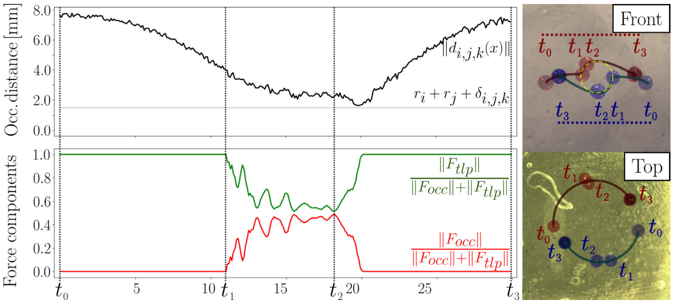

Fig. 10. Mutual occlusion avoidance (*cf. support video at 02:42*). Two microrobots (red and blue spheres) follow a circular trajectory designed to induce an occlusion in the front camera's view (Top Right). (Top Left) The projected distance between the robots (solid line) approaches the safety threshold (dotted line) defined by the HOCBF. (Bottom Left) As the robots near the occlusion point (t_1 to t_2), the autonomous controller activates a repulsive occlusion avoidance force (red line) that modifies their trajectories to ensure they remain visible, before returning full control to the teleoperation command (green line) at t3. This demonstrates the successful activation of the safety constraint. The controller activates the HOCBF safety constraint to modify the robots' paths, successfully preventing a visual occlusion without any need for operator intervention.

Tests were conducted using soft magnetic microbeads (420-C steel) and 3D-printed non-magnetic cubes, the latter designed with indentations to reduce slipping during telemanipulation. The 22 × 22 × 15 mm workspace was filled with silicone oil with viscous drag coefficient $\eta = 10^{-3}\,\mathrm{m}^2/\mathrm{s}$. For these experiments, the parameters of QP_R were tuned as follows: $\gamma = 2.0$, $k_{\alpha_{2,o_{i,j}}} = 10^9$, $k_{\alpha_{2,v_{i,l,k}}} = 10^9$, and $\delta = 25.0$.

The system successfully actuated the microrobots while satisfying the safety objectives defined in Sec. III-A (*cf. support video at 02:21*). Haptic feedback was also generated from QP_R, according to (13), providing forces and torques to support navigation guidance as well as collision and occlusion avoidance. Below, we describe representative scenarios that showcase the shared control behaviors, with particular focus on occlusion avoidance.

1) Autonomous Mutual Occlusion Avoidance: Fig. 10 displays the autonomous mutual occlusion avoidance behavior stemming from (8). The microrobots were following a clockwise circular trajectory in the XY plane, designed to systematically cause mutual occlusion in the front camera.

2) Haptic Occlusion Avoidance: Fig. 11 displays the generation of haptic occlusion avoidance feedback by QP_R. A user tries to cross the scene, with one of the two reference states x_r about to pass in an occluded area; the experiment highlights how (13) can organically transform an operator's translational motion into a rotation.

VII. DISCUSSION AND CONCLUSION

This paper introduced a multi-sensory shared control framework that enables safe and stable telemanipulation of multiple microrobots in vision-constrained environments. Our approach unified a multi-agent, optimization-based control scheme with a novel constraint-rendering technique that leverages Lagrange multipliers to provide intuitive visuo-haptic feedback. Through two user studies and a real-world hardware demonstration, we validated that our framework not only guarantees safety

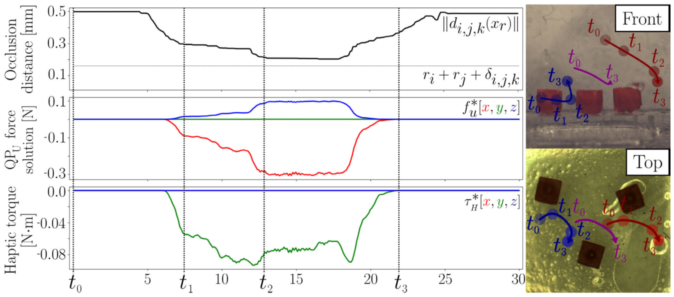

Fig. 11. Haptic occlusion avoidance (*cf. support video at 03:07*). The camera image displays the projected position of the user in the workspace (purple) and the resulting reference state x_r (blue, red). The graphs only display the blue microrobot's states for clarity. An operator attempts to move the microrobot formation through an occluded region. Initially, the reference is in a safe area and no feedback is generated (t_0). As the reference approaches the occlusion safety limit (t_1), the user-focused QP_R generates a repulsive force on the endangered reference point. This unilateral force creates a haptic torque at the end-effector (t_2), which peaks as the system guides the user away from the hazard. Once the operator's command is rotated to a safe path, the feedback is zeroed (t_3). The system automatically transforms the operator's unsafe translational command into a safe rotational maneuver by generating an intuitive torque, guiding them away from the occlusion.

from collisions and occlusions but also significantly improves operator performance in complex micromanipulation tasks.

In terms of scalability, the proposed shared-control architecture can be extended to formations of $N_\mathcal{R} > 2$ microrobots. A discussion of how a teleoperation strategy analogous to the one presented in Sec. IV-B scales to larger formations is provided in [9], where the $N_\mathcal{R}$ microrobots are arranged by equally spacing them radially around the operator-defined reference position $\boldsymbol{p}_r$. Furthermore, the scalability of the control strategy also depends on the computational properties of the controller, as well as on the characteristics of the actuation systems. Indeed, independent 3D control of multiple magnetic microrobots requires an actuation architecture capable of generating sufficiently rich magnetic fields and gradients. For $N_\mathcal{R}$ independently actuated microrobots, the number of required coil-generated degrees of freedom grows proportionally with $3N_\mathcal{R}$, which quickly leads to mechanically complex and spatially demanding hardware. Currently existing systems demonstrated simulatenous independent actuation up to three identical microrobots [44], [45].

However, even assuming independent 3D actuation, the proposed framework scales naturally to arbitrary $N_\mathcal{R}$. Indeed, the QP input dimension grows linearly as $3N_\mathcal{R} + 1$, while the number of constraints grows quadratically due to pairwise collision-avoidance and visibility constraints, as reported in Sec. III-D. To test such scalability, we performed additional stress-test simulations with $N_\mathcal{R} = 24$ microrobots and $N_\mathcal{O} = 48$ obstacles for a representative navigation task in which the agents where asked to move across the workspace while avoiding collisions, resulting in successful real-time performance with control frequency of 63 Hz.

In terms of feasibility, it is worth to observe that this may still be affected by challenging visibility conditions, even when actuation and computation remain tractable. In highly occluded environments, the image plane may become saturated by obstacles or other robots, resulting in a configuration in which safety and performance cannot be simultaneously preserved: the QP would return a feasible, safe solution that may prevent the microrobots from reaching their desired state, in view of the prioritation enforced through the *slack* variable-based mechanism. Similar issues may arise when a robot becomes trapped between obstacles or occluding structures. These effects are inherent to vision-constrained manipulation and may be mitigated through predictive control, expanded sensing modalities, or perception strategies that fuse information from more cameras to maintain triangulation.

In the future, we plan to adapt our framework to a wider set of sensors types and closing in to medical scenarios, such as ultrasound or fluoroscopy. We also intend to experiment with larger numbers of microrobots using alternative actuation techniques like optical tweezers. Finally, we aim to refine the feedback design by experimenting with multimodal haptic feedback [46] and context-aware visual cues that minimize operator fatigue while maximizing situational awareness.

REFERENCES

[1] V. Iacovacci, E. Diller, D. Ahmed, and A. Menciassi, "Medical microrobots," *Annu. Rev. Biomed. Eng.*, vol. 26, no. 1, pp. 561–591, Jul. 2024.

[2] M. A. Rahman and A. T. Ohta, "Micromanipulation with microrobots," *IEEE Open J. Nanotechnol.*, vol. 2, pp. 8–15, 2021.

[3] F. N. Piñan Basualdo and S. Misra, "Collaborative magnetic agents for 3D microrobotic grasping," *Adv. Intell. Syst.*, vol. 5, no. 12, Dec. 2023, Art. no. 2300365.

[4] N. Simaan, R. M. Yasin, and L. Wang, "Medical technologies and challenges of robot-assisted minimally invasive intervention and diagnostics," *Annu. Rev. Control, Robot., Auto. Syst.*, vol. 1, no. 1, pp. 465–490, May 2018.

[5] Y. Jin et al., "Graph neural network-based real-time 3D tracking for micro-agent control," in *Proc. Int. Conf. Manipulation, Autom. Robot. at Small Scales (MARSS)*, Jul. 2024, pp. 1–6.

[6] J. Lou et al., "Real-time trajectory tracking of a piezoelectric microrobot using asynchronous fusion of vision cameras and laser sensors," *IEEE Trans. Autom. Sci. Eng.*, vol. 22, pp. 18560–18569, 2025.

[7] L. Zheng et al., "3D navigation control of untethered magnetic microrobot in centimeter-scale workspace based on field-of-view tracking scheme," *IEEE Trans. Robot.*, vol. 38, no. 3, pp. 1583–1598, Jun. 2022.

[8] M. Christie, P. Olivier, and J.-M. Normand, "Camera control in computer graphics," *Comput. Graph. Forum*, vol. 27, no. 8, pp. 2197–2218, Dec. 2008.

[9] M. Ferro, F. N. Piñan Basualdo, P. R. Giordano, S. Misra, and C. Pacchierotti, "Experimental evaluation of haptic shared control for multiple electromagnetic untethered microrobots," *IEEE Trans. Autom. Sci. Eng.*, vol. 22, pp. 8069–8080, 2025.

[10] M. Ferro, C. Pacchierotti, S. Rossi, and M. Vendittelli, "Deconstructing haptic feedback information in robot-assisted needle insertion in soft tissues," *IEEE Trans. Haptics*, vol. 16, no. 4, pp. 536–542, Oct. 2023.

[11] X. Tan, W. S. Cortez, and D. V. Dimarogonas, "High-order barrier functions: Robustness, safety, and performance-critical control," *IEEE Trans. Autom. Control*, vol. 67, no. 6, pp. 3021–3028, Jun. 2022.

[12] L. Raphalen, M. Ferro, S. Misra, P. R. Giordano, and C. Pacchierotti, "Haptic shared control of a pair of microrobots for telemanipulation using constrained optimization," in *Proc. IEEE/RSJ Int. Conf. Intell. Robots Syst. (IROS)*, Oct. 2025, pp. 17391–17397.

[13] L. Raphalen, T. Goalard, M. Ferro, P. R. Giordano, and C. Pacchierotti, "Occlusion-safe shared micromanipulation in vision-constrained environments," in *Proc. 2nd IEEE Conf. Telepresence*, Sep. 2025. [Online]. Available: https://conf.telepresence.ieee.org/past-events/2025-2/program/

[14] L. Cinus et al., "Simplified 3D control of magnetic objects by a triple-coil static unit on a robotic arm," in *Proc. IEEE Int. Conf. Robot. Autom. (ICRA)*, 2026.

[15] C. Pacchierotti, V. Magdanz, M. Medina-Sánchez, O. G. Schmidt, D. Prattichizzo, and S. Misra, "Intuitive control of self-propelled microjets with haptic feedback," *J. Micro-Bio Robot.*, vol. 10, nos. 1–4, pp. 37–53, Oct. 2015.

[16] M. Mehrtash and M. B. Khamesee, "Micro-domain force estimation using Hall-effect sensors for a magnetic microrobotic station," *J. Adv. Mech. Design, Syst., Manuf.*, vol. 7, no. 1, pp. 2–14, 2013.

[17] C. Pacchierotti et al., "Steering and control of miniaturized untethered soft magnetic grippers with haptic assistance," *IEEE Trans. Autom. Sci. Eng.*, vol. 15, no. 1, pp. 290–306, Jan. 2018.

[18] C. Huang, T. Xu, D. Li, and X. Wu, "Cooperative control strategy of multiple magnetic millirobots for automatic assembly," *IEEE/ASME Trans. Mechatronics*, vol. 30, no. 5, pp. 3572–3583, Oct. 2025.

[19] V. Hamdipoor, M. Afzal, T.-A. Le, and J. Yoon, "Haptic-based manipulation scheme of magnetic nanoparticles in a multi-branch blood vessel for targeted drug delivery," *Micromachines*, vol. 9, no. 1, p. 14, Jan. 2018.

[20] S. Zhong et al., "Spatial constraint-based navigation and emergency replanning adaptive control for magnetic helical microrobots in dynamic environments," *IEEE Trans. Autom. Sci. Eng.*, vol. 21, no. 4, pp. 7180–7189, Oct. 2024.

[21] T. Xu, C. Huang, Z. Lai, and X. Wu, "Independent control strategy of multiple magnetic flexible millirobots for position control and path following," *IEEE Trans. Robot.*, vol. 38, no. 5, pp. 2875–2887, Oct. 2022.

[22] S. Zhong et al., "Paired interactions of magnetic millirobots in confined spaces through data-driven disturbance rejection control under global input," *IEEE/ASME Trans. Mechatronics*, vol. 30, no. 6, pp. 6688–6699, Dec. 2025.

[23] G. T. McKee and P. S. Schenker, "Human–robot cooperation for automated viewing during teleoperation," in *Proc. IEEE/RSJ Int. Conf. Intell. Robots Syst., Hum. Robot Interact. Cooperat. Robots*, vol. 1, Aug. 1995, pp. 124–129.

[24] N. Maeda, J. Morita, and M. Sugimoto, "Pathfinder vision: Teleoperation robot interface in consideration of geometry for supporting future prediction," in *Proc. ACM SUI*, 2014, pp. 29–35.

[25] D. Rakita, B. Mutlu, and M. Gleicher, "Remote telemanipulation with adapting viewpoints in visually complex environments," in *Proc. Robotics, Sci. Syst. (RSS)*, 2019. [Online]. Available: https://www.roboticsproceedings.org/rss15/p68.html

[26] X. Xiao, T. Smith, and R. R. Murphy, "Tethered aerial visual assistance," 2020, *arXiv:2002.05963*.

[27] M. M. Shilleh, Q. A. Amer, J. Dufek, and R. R. Murphy, "Best and worst external viewpoints for teleoperation visual assistance," in *Proc. Companion ACM/IEEE Int. Conf. Hum.-Robot Interact.*, Mar. 2021, pp. 675–676.

[28] R. Jia, L. Yang, Y. Cao, C. Kalun Or, W. Wang, and J. Pan, "Learning autonomous viewpoint adjustment from human demonstrations for telemanipulation," *ACM Trans. Hum.-Robot Interact.*, vol. 13, no. 3, pp. 1–23, Sep. 2024.

[29] I. Chuang et al., "Active vision might be all you need: Exploring active vision in bimanual robotic manipulation," 2024, *arXiv:2402.01234*.

[30] B. Omarali, B. Denoun, K. Althoefer, L. Jamone, M. Valle, and I. Farkhatdinov, "Virtual reality based telerobotics framework with depth cameras," in *Proc. 29th IEEE Int. Conf. Robot Human Interact. Commun. (RO-MAN)*, Aug. 2020, pp. 1217–1222.

[31] S. Kuitert, J. Hofland, C. J. M. Heemskerk, D. A. Abbink, and L. Peternel, "Orbital head-mounted display: A novel interface for viewpoint control during robot teleoperation in cluttered environments," in *Proc. IEEE/RSJ Int. Conf. Intell. Robots Syst. (IROS)*, Oct. 2023, pp. 1–7.

[32] P. Praveena, L. Molina, Y. Wang, E. Senft, B. Mutlu, and M. Gleicher, "Understanding control frames in multi-camera robot telemanipulation," in *Proc. 17th ACM/IEEE Int. Conf. Hum.-Robot Interact. (HRI)*, Mar. 2022, pp. 432–440.

[33] T.-C. Lin, A. Unni Krishnan, and Z. Li, "Perception-motion coupling in active telepresence: Human behavior and teleoperation interface design," *ACM Trans. Hum.-Robot Interact.*, vol. 12, no. 3, pp. 1–24, Sep. 2023.

[34] F. Ongaro, S. Pane, S. Scheggi, and S. Misra, "Design of an electromagnetic setup for independent three-dimensional control of pairs of identical and nonidentical microrobots," *IEEE Trans. Robot.*, vol. 35, no. 1, pp. 174–183, Feb. 2019.

[35] A. D. Ames, X. Xu, J. W. Grizzle, and P. Tabuada, "Control barrier function based quadratic programs for safety critical systems," *IEEE Trans. Autom. Control*, vol. 62, no. 8, pp. 3861–3876, Aug. 2017.

[36] E. D. Sontag, "A Lyapunov-like characterization of asymptotic controllability," *SIAM J. Control Optim.*, vol. 21, no. 3, pp. 462–471, May 1983.

[37] H. Khalil, *Nonlinear Systems*. New York, NY, USA: Macmillan, 2002.

[38] J. Rawlings and D. Mayne, *Model Predictive Control: Theory and Design*. Madison, WI, USA: Nob Hill Publishing, 2009.

[39] W. Xiao, C. G. Cassandras, and C. Belta, *Safe Autonomy With Control Barrier Functions: Theory and Applications*. Cham, Switzerland: Springer, 2023.

[40] S. P. Boyd and L. Vandenberghe, *Convex Optimization*. Cambridge, U.K.: Cambridge Univ. Press, 2004.

[41] R. Rahal, A. M. Ghalamzan-E.,F. Abi-Farraj, C. Pacchierotti, and P. Robuffo Giordano, "Haptic-guided grasping to minimise torque effort during robotic telemanipulation," *Auto. Robots*, vol. 47, no. 4, pp. 405–423, Apr. 2023.

[42] E. A. Rakhmanov, E. B. Saff, and Y. M. Zhou, "Minimal discrete energy on the sphere," *Math. Res. Lett.*, vol. 1, no. 6, pp. 647–662, 1994.

[43] S.-C. Hsu, X. Xu, and A. D. Ames, "Control barrier function based quadratic programs with application to bipedal robotic walking," in *Proc. Amer. Control Conf. (ACC)*, Jul. 2015, pp. 4542–4548.

[44] R. Khalesi, H. Nejat Pishkenari, and G. Vossoughi, "Simultaneous and independent control of multiple swimming magnetic microrobots by stabilizer microrobot," *J. Intell. Robotic Syst.*, vol. 110, no. 2, p. 70, May 2024.

[45] S. Chowdhury, W. Jing, and D. Cappelleri, "Towards independent control of multiple magnetic mobile microrobots," *Micromachines*, vol. 7, no. 1, p. 3, Dec. 2015.

[46] C. Pacchierotti and D. Prattichizzo, "Cutaneous/tactile haptic feedback in robotic teleoperation: Motivation, survey, and perspectives," *IEEE Trans. Robot.*, vol. 40, pp. 978–998, 2024.

Leon Raphalen received the first master's degree in aeronautics and astronautics from NCKU, Tainan, Taiwan, in 2018, and the second master's degree in aerospace engineering from IPSA, Paris, France, in 2019. He is currently pursuing the Ph.D. degree with CNRS, Rennes, France. He spent several years working in the automotive industry around the field of embedded software for autonomous driving before resuming his studies, and he explores the fields of control theory, shared control, and microrobotics.

Marco Ferro received the Ph.D. degree in automation, bioengineering and operational research from Sapienza University of Rome, Italy, in 2019. He has been a Post-Doctoral Researcher with CNRS, IRISA, Rennes, France, since 2022. Previously, he was a Post-Doctoral Researcher with the Department of Computer, Control, and Management Engineering (DIAG), Sapienza University of Rome. Throughout his experience, he worked on vision-based methods for mobile and surgical robots, shared control, and estimation/rendering techniques in medical robotics.

Nicholas R. Posselli received the Ph.D. degree in mechanical engineering from the University of Utah, Salt Lake City, UT, USA, in 2024, with a focus on robotic assistance for retinal surgery. He is currently a Post-Doctoral Researcher with the Department of Biomechanical Engineering, University of Twente, Enschede, The Netherlands. His current research interests include magnetic manipulation and the development of small- and large-scale magnetic actuation systems for medical applications.

Paolo Robuffo Giordano (Senior Member, IEEE) received the Ph.D. degree in systems engineering from the University of Rome "La Sapienza" in 2008. In 2007, he spent one year as a Post-Doctoral Researcher with the Institute of Robotics and Mechatronics, German Aerospace Center (DLR). From 2008 to 2012, he was a Senior Research Scientist with the Max Planck Institute for Biological Cybernetics, Tübingen, Germany. He is currently a Senior CNRS Researcher and the Head of the Rainbow Group, IRISA, Rennes, France.

Sarthak Misra (Senior Member, IEEE) received the Ph.D. degree in mechanical engineering from Johns Hopkins University, Baltimore, MD, USA, in 2009. He is currently a Professor with the Department of Biomechanical Engineering, University of Twente, Enschede, The Netherlands, and the Department of Biomedical Engineering, University of Groningen, Groningen, The Netherlands. He is also the Co-Chair of the IEEE RAS Technical Committee on Surgical Robotics and the IFAC Technical Committee on Biological and Medical Systems.

Claudio Pacchierotti (Senior Member, IEEE) received the Ph.D. degree from the University of Siena in 2014. He has been a tenured Researcher with CNRS, IRISA, Rennes, France, since 2016. Previously, he was a Post-Doctoral Researcher with Italian Institute of Technology, Genoa, Italy. He received the 2014 EuroHaptics Best Ph.D. Thesis Award and the 2022 CNRS Bronze Medal. He is the Co-Chair of the IEEE Technical Committee on Telerobotics, the Associate Vice President of the IEEE RAS Technical Activities Board, and the Secretary of the Eurohaptics Society.